# Magnetism and plasmonic performance of mesoscopic hollow ceria spheres decorated with silver nanoparticles

Eric Nestor Tseng, Yin-Ting Hsiao, Yi-Che Chen, Shih-Yun Chen, Alexandre Gloter, Jenn-Ming Song

## To cite this version:

Eric Nestor Tseng, Yin-Ting Hsiao, Yi-Che Chen, Shih-Yun Chen, Alexandre Gloter, et al.. Magnetism and plasmonic performance of mesoscopic hollow ceria spheres decorated with silver nanoparticles. Nanoscale, 2019, 11 (8), pp.3574-3582. ⟨10.1039/C8NR09636H⟩. ⟨hal-02323633⟩

**HAL Id: hal-02323633**
**https://hal.science/hal-02323633v1**

Submitted on 13 Nov 2020

**HAL** is a multi-disciplinary open access archive for the deposit and dissemination of scientific research documents, whether they are published or not. The documents may come from teaching and research institutions in France or abroad, or from public or private research centers.

L'archive ouverte pluridisciplinaire **HAL**, est destinée au dépôt et à la diffusion de documents scientifiques de niveau recherche, publiés ou non, émanant des établissements d'enseignement et de recherche français ou étrangers, des laboratoires publics ou privés.

Autorisation HAL

HAL Authorization

View Article Online
View Journal

# Nanoscale

## Accepted Manuscript

This article can be cited before page numbers have been issued, to do this please use: E. N. Tseng, Y. Hsiao, Y. Chen, S. Chen, A. Gloter and J. Song, *Nanoscale*, 2019, DOI: 10.1039/C8NR09636H.

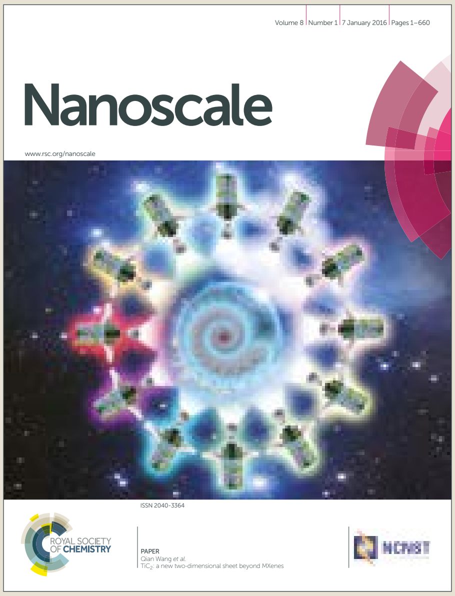

Volume 8 | Number 1 | 7 January 2016 | Pages 1–660

Nanoscale

www.rsc.org/nanoscale

ISSN 2040-3364

ROYAL SOCIETY OF CHEMISTRY

PAPER
Qian Wang et al.
$TiC_2$: a new two-dimensional sheet beyond MXenes

NCNST

This is an Accepted Manuscript, which has been through the Royal Society of Chemistry peer review process and has been accepted for publication.

Accepted Manuscripts are published online shortly after acceptance, before technical editing, formatting and proof reading. Using this free service, authors can make their results available to the community, in citable form, before we publish the edited article. We will replace this Accepted Manuscript with the edited and formatted Advance Article as soon as it is available.

You can find more information about Accepted Manuscripts in the author guidelines.

Please note that technical editing may introduce minor changes to the text and/or graphics, which may alter content. The journal's standard Terms & Conditions and the ethical guidelines, outlined in our author and reviewer resource centre, still apply. In no event shall the Royal Society of Chemistry be held responsible for any errors or omissions in this Accepted Manuscript or any consequences arising from the use of any information it contains.

ROYAL SOCIETY OF CHEMISTRY

rsc.li/nanoscale

View Article Online
DOI: 10.1039/C8NR09636H

# Magnetism and plasmonic performance of mesoscopic hollow ceria spheres decorated with silver nanoparticles

Eric Nestor Tseng[1], Ying-Ting Hsiao[1], Yi-Che Chen[1], Shih-Yun Chen[1, *], Alexandre Gloter[2, *] and Jenn-Ming Song[3]

[1] Department of Materials Science and Engineering, National Taiwan University of Science and Technology, Taipei, Taiwan

[2] Laboratoire de Physique des Solides, Université Paris Sud, CNRS UMR 8502, F-91405 Orsay, France

[3] Department of Materials Science and Engineering, National Chung Hsing University, Taichung 402, Taiwan

Published on 07 January 2019. Downloaded on 1/21/2019 12:35:13 AM.

Nanoscale Accepted Manuscript

We investigate the role of interfaces and surfaces on the magnetic and surface enhanced Raman spectroscopy (SERS) properties of $CeO_2$ hollow spheres decorated by Ag nanoparticles (H-$CeO_2$@Ag). The composites, H-$CeO_2$@Ag, were synthesized using a newly developed two-step process. The $CeO_2$ hollow sphere diameter ranges from 100 nm to 2 μm and the grafted Ag nanoparticles (NP) size varies from 5 to 50 nm with a controllable coverage ratio. Spectroscopic and microscopic characterization confirms the formation of an interface between the Ag and ceria and shows different charge rearrangements occurring at both the interface and surface. Room temperature ferro-magnetism was observed in all composites, and is associated mostly with ceria surface defects.

Strong SERS effect was reported with a detection limit down to $10^{-14}$ M for rhodamine 6G analytes. Scanning transmission electron microscopy and electron energy loss spectroscopy investigation reveals that hot-spots are associated with the silver NPs surfaces and also with Ag/ $CeO_2$ interface. This interfacial hot spot occurs for metallic particles above 30 nm and is strongly red shifted with respect to the Ag surface plasmon. The strong SERS activity is then attributed to the presences of several types of hot-spots and the geometrical features (buoyant hollow sphere, size dispersion) of the composite.

## Introduction

Ceria ($CeO_2$) based materials possess several unusual properties due to the occurrence of oxygen vacancies. It has a high oxygen storage capacity and can have a stable structure far from the stoichiometric proportions of oxygen. When the ceria material size is decreased, the oxygen vacancies tend to aggregate at the surface.[1, 2] All of these characteristics present a wide range of

View Article Online
DOI: 10.1039/C8NR09656H

ceria-based nano-material applications in the catalyst field such for carbon monoxide oxidation[3] and solid-oxide-fuel-cell electrolytes.[4] The catalytic behavior can be further improved with the addition of noble metals, such as Au,[5] Ag,[6, 7] Cu [8] and Pt.[9] In those metal/$CeO_2$ catalysts, the improvement was attributed to the new active site at the metal-support interface,[10] the mediated activation of $O_2$ by the formation of oxygen vacancies in the support,[11] and the formation of superoxide species during the redox process.[12, 13] More recently nanostructured ceria or metal/ceria hybrids have been investigated in other contexts such as the occurrence of ferromagnetism [14] or its capability to increase the SERS activity of metal nano particles.[15]

The introduction of defects converts $CeO_2$ into ferromagnetic at room temperature.[16] Several types of defects were reported such as dopants, oxygen vacancies or nano-structuration (high surface to volume ratio, presence of grain boundaries or interfacing). Magnetic and non-magnetic dopants and oxygen vacancies (inducing some $Ce^{3+}$) could contribute to magnetic exchange as demonstrated by Electron paramagnetic resonance (EPR) and X-ray magnetic circular dichroism (XMCD).[17, 18] During the past decade, the nature of these point defects including the type, concentration, structure and distribution was studied using various methods and correlated to the magnetic behavior.[19, 20] Several models have been developed to explain the ferromagnetism,[21-23] however, all of them relate primarily to the interplay of $Ce^{3+}$ with the defects at its origin. Furthermore, introducing interfaces using metallic particles deposition onto ceria substrates is also an efficient way to engineer the interplay of $Ce^{3+}$ with defects.[24, 25] At the interface charge re-distribution between cerium and nearby noble metals such as Ag, Au and Pt have been found.[26-28] For example, it has been demonstrated that after depositing $CeO_2$ NPs onto an Ag core, a $Ce^{3+}$- rich defective layer was observed at the interface between Ag and $CeO_2$. The $Ce^{3+}$ concentration reached 40% at the interface, which is consistent with the optimum concentration and benefit for magnetic exchange.[14]

Concerning the SERS properties, a recent study demonstrated that $CeO_2$-on-Ag particles exhibit a $CeO_2$ thickness-dependent SERS effect in which their best SERS effect is 2 orders stronger than that of Ag particles.[15] Such electromagnetic field enhancement due to metal interfacing with a semiconductor has also been reported for $CuO_2$/Ag,[29] $Fe_2O_3$/Ag[30] and $TiO_2$/Ag[31] but its origin is still debated. It has been suggested that the electronic effect due to charge transfer between the metal and the semi-conductor changes the SERS intensity and red-shifts the extinction spectra.[29] Total-field scattered-field calculations reveal that nanostructures made of semiconductor and metallic nanoparticles give origin to complex field enhancement near the interface without the requirement of such electronic reconstruction.[32, 33]

Published on 07 January 2019. Downloaded on 1/21/2019 12:35:13 AM.

Nanoscale Accepted Manuscript

View Article Online
DOI: 10.1039/C8NR09636H

$CeO_2$ sub-micrometer hollow spheres covered with Ag nanoparticles on the surface were synthesized in this study utilizing a newly developed two-step method. We reported that Ag nanoparticles with typical size of 10 nm attached to the ceria surface with a coverage ratio ranging from 0.1 to 0.4 depending on the synthesis parameters. Spectroscopic measurements confirm that a charge transfer occur at the Ag / $CeO_2$ interface. With increased Ag concentration, the magnetic properties exhibit a maximum value but further investigations indicated that such maximum value arises from surface modification in the ceria hollow sphere resulting from the Ag chemical deposition. This study indicates that charge transfer at the Ag / $CeO_2$ interface can be active or inactive for FM depending on the exact number of charges at the interface. The SERS performance was evaluated on Rhodamine 6G (R6G) detection and found optimal for coverage ratio of ca. 0.2. The detection limit and enhancement factor (EF) are then as high as $1\times10^{-14}$ M and $4.8\times10^{11}$. The STEM-EELS investigation verified the presence of hot spots associated with silver particles, and also to SERS hotspots at the $CeO_2$−Ag interfaces whose plasmon band energy is interestingly in resonance with the Raman laser excitation sources (532 nm). This hollow structure provides buoyant ability and wide size distribution that improves dispersion in solution, both resulting in contact area enhancement with the analytes. Such hollow ceria sphere – silver composites are then promising "lab-on-a-bubble (LoB)" SERS material.[33]

## Experimental procedure

### *Sample preparation*

Two-step process was used to obtain H-$CeO_2$@Ag composites. At first, hollow $CeO_2$ spheres were prepared using the spray pyrolysis method (SP). Ceric ammonium nitrate (CeAN, $(NH_4)_2$ $Ce(NO_3)_6$, 99.5%, Alfa Aesar) and Glycine (GN, $C_2H_5NO_2$, 98%, Acros Organics) were used as precursor. $CeO_2$ particles were prepared firstly from a 1 wt% solution CeAN and GN in de-ionized water with molar ratio of 4:6. The precursor solution was atomized into small droplet at first (nebulizer, King Ultrasonics Co., Ltd, Taipei, Taiwan) and then underwent solvent evaporation, solute precipitation and precursor decomposition in the heated tubular reactor at 700°C in atmosphere. Hollow $CeO_2$ spheres were collected using a cylindrical electrostatic collector with high voltage potential and then annealed in air at 300°C for 2 hours. Silver nanoparticles were deposited on the annealed hollow $CeO_2$ spheres via the incipient wetness method using silver nitrite ($AgNO_3$) as the precursor. The hollow $CeO_2$ sphere and $AgNO_3$ mixture was then calcined at 300°C for 3 hours. The prepared H-$CeO_2$@Ag composites were then cleaned using centrifugation several times and then dried at room temperature.

### *Characterization*

Published on 07 January 2019. Downloaded on 1/21/2019 12:35:13 AM.

Nanoscale Accepted Manuscript

View Article Online
DOI: 10.1039/C8NR09636H

All NPs were characterized by X-ray Diffractometer (XRD) with Cu *K* radiation (Bruker D8 Advance). The morphology was investigated using transmission electron microscopy (TEM) operated at 200 keV (FEI-TEM, Tecnai G2). The hollow sphere shell thickness was estimated based on 100 measurements. Scanning transmission electron microscope (STEM), high angle annular dark field (HAADF) and electron energy loss spectroscopy were acquired using a Cs corrected STEM NION operated at 60 keV to limit the electron damage. X-ray absorption measurements were carried out at National Synchrotron Radiation Research Center (NSRRC) in Taiwan. The X-ray absorption near edge structure (XANES) spectroscopy measurements at the Ce $L_3$-edge were performed at Wigger beam line 17C at room temperature through a monochromator silicon (111) crystal. The energy resolution at the Ce $L_3$-edge (5723 eV) was approximately 0.4 eV. The XANES spectra at the Ag *K*-edge was recorded at HSGM beam line 01C and the energy resolution was set to 1.25 eV. Raman scattering spectrometer equipped micro Raman system (HORIBA iHR550) and a diode laser at an excitation wavelength of 532 nm. The magnetization was measured at room temperature using a vibrating sample magnetometer (VSM) at the Institute of Physics, Academia Sinica, Taiwan.

Published on 07 January 2019. Downloaded on 1/21/2019 12:35:13 AM.

Nanoscale Accepted Manuscript

## Results and discussion

### *Hollow-$CeO_2$ spheres*

Figures 1 (a) and (b) are TEM images of $CeO_2$ spheres prepared using the spray pyrolysis method, showing that all spheres are hollow and the shell thickness is about 30 nm. The diffraction pattern in the inset of Fig. 1 (a) confirms that the spheres are $CeO_2$. The $CeO_2$ sphere size distribution is plotted in the inset of Fig. 1 (b), showing that the $CeO_2$ sphere diameter ranges from 100 nm to 2 μm. As seen in Fig. 1 (c), the shell is composed of well crystallized $CeO_2$ particles with a size between 4 to 6 nm and the dominant surfaces are [111].

The hollow $CeO_2$ spheres (H-$CeO_2$) concentration defect was investigated by estimating the bulk valence of Ce using the Ce *L*-edge X-ray absorption near-edge structure (XANES). The spectra as well as the quantification procedure are plotted in Fig. S1, a $Ce^{3+}$ concentration of about 10% was found. The Ce-M edge measured by EELS was utilized to reveal the $Ce^{3+}$ distribution throughout the hollow $CeO_2$ spheres. As seen in Fig. 1 (d)-(f), the $Ce^{3+}$ distribution is inhomogeneous. It tends to aggregate at the surface region in these spheres. As the distance from the surface increases from 0 to 2.4 nm, the $Ce^{3+}$ concentration determined by EELS decreases gradually from ca. 25% to 12%. This data is in a fair agreement with the XAS bulk estimation.

### *Hollow-$CeO_2$ @Ag composites*

View Article Online
DOI: 10.1039/C8NR09636H

Published on 07 January 2019. Downloaded on 1/21/2019 12:35:13 AM.

Nanoscale Accepted Manuscript

The obtained hollow $CeO_2$ spheres were then used as the substrate to grow Ag NPs. The size as well as the Ag NPs distribution was adjusted by varying the Ag concentration in the precursor. The Ag to $CeO_2$ mole ratio was set to 0.33, 0.5, 0.71, 0.83, and 0.91. The obtained H-$CeO_2$@Ag composite was named samples I, II, III, IV and V, respectively. XRD analysis of H-$CeO_2$@Ag composites is illustrated in Fig. 2 (a). All patterns can be identified as the fluorite structure of $CeO_2$ (JCPDS 34-0394) and Ag (JCPDS 04-0783). No peaks corresponding to other phases were detected. TEM investigations of samples II, IV and V are shown in Fig. 2 (b)-(d), demonstrating that there are nanoparticles randomly distributed on the hollow sphere's surface. According to the high resolution TEM of interface region (Fig. 2 (e)) and the compositional analysis obtained on sample IV (shown in Fig. S2), it is confirmed that the spheres are $CeO_2$ and the nanoparticles on the surface are Ag. It was also observed that the micro-features of Ag NPs are closely related to the Ag/$CeO_2$ concentration ratio. The size and inter-particle spacing of Ag NPs as well as the ratio of coverage, $A_{Ag}/A_{CeO2}$, among H-$CeO_2$@Ag composites were then compared, where $A_{Ag}$ is the interface area between Ag and $CeO_2$ and $A_{CeO2}$ is the surface area of the hollow $CeO_2$ sphere. In Figs. 2 (f) and (g), two-step change is observed. As the Ag/$CeO_2$ concentration ratio is lower than 0.71, both the size and inter-particle spacing is almost the same. With further Ag/$CeO_2$ concentration ratio enhanced from 0.71 to 0.91, the change in morphology of the composites is obvious. In sample V, both the size and amount of Ag particle increase, forming a nearly continuous Ag layer on the surface. The micro-feature evolution of Ag NPs results in the monotonously increasing coverage ratio (Fig. 2 (h)).

The H-$CeO_2$ defect concentration after depositing Ag was investigated using Ce *L*-edge XANES (shown in Fig. S3). The estimated results show that the bulk $Ce^{3+}$ concentration increases from 10% to 11% after Ag NPs deposition. Further increasing the Ag content, it is interesting that there is no obvious difference in the $Ce^{3+}$ concentration among samples I to V.

The Ce valence spatial distribution after Ag NPs deposition was investigated using EELS. The Ce *M* edge obtained from the exposed surface, interface between Ag NP and $CeO_2$ sphere, and the bulk of $CeO_2$ sphere were compared, which was present as spectra 1, 2, and 3, respectively in Figs. 3 (a) and (b). The edge features vary among these positions, implying inhomogeneity in the $Ce^{3+}$ distribution. The $Ce^{3+}$ distribution was demonstrated by the mapping (Fig. 3 (c)) and line profile (Fig. 3 (d), where line A cross the interface between Ag NP and $CeO_2$ spheres, while line B crosses the exposed surface of the $CeO_2$ sphere. This shows that at surface regions without Ag NPs, the $Ce^{3+}$ aggregates within a narrow surface region of ca. 1.7 nm where the concentration can be as high as ca. 50%. On the other hand, in regions covered by Ag NPs, the aggregation of $Ce^{3+}$ at the surface is not

View Article Online
DOI: 10.1039/C8NR09636H

Published on 07 January 2019. Downloaded on 1/21/2019 12:35:13 AM.

Nanoscale Accepted Manuscript

as obvious as those regions without Ag coverage. The $Ce^{3+}$ concentration in this region is only 25% with a $Ce^{3+}$ rich region reduced to 1 nm.

The $Ce^{3+}$ aggregation at sphere surface, including the exposed surface and the interface between Ag NP and $CeO_2$ sphere, can be attributed to the Ag deposition process. During the deposition process, hollow $CeO_2$ spheres were heated to 300°C in air and last for 2 hours, which leads to the migration of oxygen vacancies to the surface. As for the difference between the exposed surface and the interface region, it may be caused by several reactions. At the exposed surface, the interaction with acid solution ($Ag^+$ and $NO_3^-$) also contributes to the increase in $Ce^{3+}$. At the interface, charge transfer with the silver or to a surface oxidation of ceria during the chemical $Ag^+ \rightarrow Ag^0$ conversion should be considered. Several works reported on the charge transfer at $CeO_2$/Ag interfaces but they reported that electrons are transferred from the silver to the ceria surface, which is contradictory to our finding. The XANES measurement of the Ag-*L* and Ag-*K* edges (shown in Fig. S4) indicate that the silver electronic structure is modified by the interface with ceria (an increase of the Ag-*d* band population is observed). Nevertheless, the change is small and the electronic reconstruction at the interface might not be the primary source of the weaker $Ce^{3+}$ at the interface. The occurrence of charge transfer at the interface between Ag and $CeO_2$ here plays a minor role. As a consequence, at the interface between Ag and $CeO_2$ spheres the $Ce^{3+}$ concentration is less compared to the surface.

The defect structure was further investigated by Raman spectroscopy. As seen in Fig. 4 (a), two bands were detected. The first band around 456 $cm^{-1}$ is an $F_{2g}$ mode and is due to the symmetric stretching vibration mode of oxygen and cerium atoms. Its energy position is slightly altered with depositing Ag NPs. The second band (*D* band) starts from 520 $cm^{-1}$ to 670 $cm^{-1}$ and can be decomposed into two peaks which center at 560 $cm^{-1}$ ($D_1$) and 600 $cm^{-1}$ ($D_2$). The $D_1$ peak is assigned to defect species including $Ce^{3+}$ with a neighboring oxygen vacancy, while the $D_2$ peak is related to defect species including a trivalent cation ($M^{3+}$) without any oxygen vacancy, id est, maintaining an $O_h$ symmetry around $M^{3+}$.[34] The D band fitting results are plotted in Figs. 4 (b) and (c). Before silver deposition, the D band presents a very weak intensity. It becomes more intense with Ag deposition on the ceria surface, notably because the metallic nanoparticles increase the surface contribution of the Raman signal where defects are more present. When the amount of silver increases, the increase in $D/F_{2g}$ ratio confirms the surface is enriched in defects. In particular, the $D_1$ peak growth indicates that the dominant defect species induced by Ag deposition is the $Ce^{3+}$-$V_o$ type.

## *Magnetic behavior*

Composite M-H curves as well as bare Ag particles and hollow $CeO_2$ spheres measured by

View Article Online
DOI: 10.1039/C8NR09656H

VSM at room temperature are reported in Fig. 5 (a). The diamagnetic signal of sample holder and paramagnetic component of specimen were subtracted from all magnetization curves. Clear hysteresis loops are observed in this figure, showing that all samples are ferromagnetic with the value of coercivity, $H_c$, ranging from 300 to 400 Oe, while $M_s$ varies over one order of magnitude. In H-$CeO_2$, $M_s$ is 0.0005 emu/g and is then enhanced with Ag deposition. The $M_s$ of all composites is indeed higher than that of both bare H-$CeO_2$ and bare Ag NPs. Furthermore, the increment is not linear with the Ag content. A dramatic change is observed within a narrow range as the Ag/Ce ratio increases from 0.71 to 0.91.

Both Ag NPs and $CeO_2$ could be contributor to FM. In the case of silver nanoparticles, the origin of FM is still controversial. The reconstruction of surface structure[35-37] and surface oxidation[37] has been suggested to result in the FM. For the ceria or titania that are primary nonmagnetic oxides, FM formation has been associated with the presence of defects. In ceria, a strong correlation between the ferromagnetism enhancement and the amount of $Ce^{3+}$ has been demonstrated. [16, 24,38] Notably, in H-$CeO_2$@Ag composites, three types of $CeO_2$ regions with different $Ce^{3+}$ concentrations were revealed by the STEM/EELS analysis (inset of Fig. 5 (b)). Region A is the bulk of H-$CeO_2$ sphere, where the $Ce^{3+}$ concentration is low. Region B is the interface between Ag NPs and H-$CeO_2$ spheres, where the $Ce^{3+}$ concentration is controlled by the oxygen vacancy migration and charge transfer between Ag and $CeO_2$. Region C is the H-$CeO_2$ surface, where the $Ce^{3+}$ concentration depends on both the oxygen vacancy migration and the interaction between the ceria and acidic solution. According to the concentration of $Ce^{3+}$, both region B and C is beneficial for the FM enhancement. Notably, the ratios between these three regions changes when the Ag/Ce concentration is increased.

To demonstrate the role each part plays in the FM enhancement, the increment of the Ag/H-$CeO_2$@Ag weight ratio, the Ag/$CeO_2$ interface area (region B), and the $M_s$ with changing Ag/Ce mole ratio are shown in Fig. 5 (b). At first, no obvious difference is observed in both the weight ratio and the interface area until the Ag/Ce mole ratio reaches 0.71, while a linear growth is seen as further enhance the Ag/Ce mole ratio to 0.91. As for the variation trend of $M_s$, a larger increment is seen, in particular of composites with higher concentrations of Ag. However, it decreases as further enhance the Ag/Ce mole ratio to above 0.83. The strongest $M_s$ is obtained when neither the deposited silver nor the coverage is the maximum. This indicates that the strongly reduced H-$CeO_2$ sphere surface (region C) is the prime contributor to FM enhancement.

The surface effect of the ceria hollow sphere over the interfacial effect with silver for the magnetic properties was controlled by investigating the magnetic properties of pure hollow spheres

Published on 07 January 2019. Downloaded on 1/21/2019 12:35:13 AM.

Nanoscale Accepted Manuscript

View Article Online
DOI: 10.1039/C8NR09636H

Published on 07 January 2019. Downloaded on 1/21/2019 12:35:13 AM.

Nanoscale Accepted Manuscript

where no Ag NPs have been deposited but whose chemical and physical treatment were made as close as possible for silver deposition. The results are shown in Fig. S5 where the magnetic properties as a function of the salt concentration exhibit a similar narrow peak for a salt concentration similar to the optimum for Ag deposition. This confirms the role of surface $Ce^{3+}$ aggregation on the hollow sphere for $M_s$ enhancement.

### *SERS performance*

Magnetic NP field enhancement and its SERS performance can be maximized by tailoring the nano-features of metallic particles, including the shape, size and arrangement.[39-41] As mentioned in the introduction, covering $CeO_2$ onto Ag particles might also be a way to improve the SERS performance.[15] Nevertheless, the exact role of $CeO_2$ on the SERS properties is not yet understood.

The SERS effect of H-$CeO_2$@Ag composites were then estimated on typical analytes Rhodamine 6G (R6G). The H-$CeO_2$@Ag composite detection process is illustrated in the inset of Fig. 6 (a). The SERS spectrum of H-$CeO_2$@Ag composite is shown in Fig. 6 (b) (sample IV) and Fig. S6 (others), where the R6G concentration was set to $1\times10^{-6}$ M. The typical Raman peaks at 1310, 1363, 1509, 1572 and 1650 $cm^{-1}$ are clear and in accordance with the reported values.[42] The SERS detection limit of sample IV was then examined by decreasing the R6G concentration from $1\times10^{-6}$ to $1\times10^{-14}$ M. A plot of the R6G concentration vs. signal intensity for the band at 1663 $cm^{-1}$ is shown in the inset, demonstrating that the SERS signal can be detected even when the R6G concentration is as low as $1\times10^{-14}$ M. EF was calculated using the standard formula,[43] $\mathrm{EF} = \frac{I_{SERS}C_0}{I_o C_{SERS}}$, where $I_0$ and $C_0$ determine the Raman measurement peak intensity and the concentration with the reference R6G solution; $I_{SERS}$ and $C_{SERS}$ present the peak intensity and the SERS sample concentration. The most intense peak was considered for EF calculation. The EF has a maximum value for sample IV and it is then as high as $4.8\times10^{11}$. Such value is much higher than that provided by Ag colloid or the Ag-coated LoBs using coupling agents (about $2.3\times10^{7}$).[44]

Now regarding the morphological difference between the samples, as seen in Fig. 2, the inter-particle spacing between Ag particles is smaller for samples IV and V compared to samples with lower Ag/$CeO_2$ mole ratios. Comparing samples IV and V, the latter has larger Ag particles and larger $CeO_2$ coverage. This seems to indicate that Ag particle surfaces and also the interactions with the $CeO_2$ surfaces are important for SERS performance.

The plasmonic behavior of Ag particles with different sizes (about 10 nm and 40 nm) on $CeO_2$ spheres were investigated experimentally utilizing STEM-EELS. Figure 7 shows the EELS spectra

View Article Online
DOI: 10.1039/C8NR09636H

and the EELS intensity spatial distribution for two energy windows of H-$CeO_2$@Ag composites with small Ag particles on their surfaces. Spectrum 1 has a strong maximum at ca. 3.2 eV that is typical for a spherical Ag surface plasmon of ca. 10nm.[48] Spectrum 3 is from the ceria surface and exhibits a strong onset at around 3.5 eV that corresponds to the ceria band gap.[49] Spectrum 2 is obtained at a few nanometers from the ceria surface and in-between two Ag particles. It shows a peak for the Ag surface plasmon and the signal from the neighboring ceria surface. The peak of the Ag surface plasmon is a bit broader than at spectrum 1 and exhibits high and low energy shoulders. Such additional features are coming from a small coupling effect between the 2 particles. Their exact intensities and energies depend on the geometrical aspects (size, inter-particle spacing, rotation of the dimers with respect of the electron beam, substrate proximity, ...).[47, 48]

For H-$CeO_2$@Ag composites with large Ag particles (Fig. 7), in addition to the above plasmon modes, another mode appears at around 2.1 - 2.5 eV (spectrum 7). It was detected with a strong intensity at the corner between large Ag particle (> 20nm) and the ceria sphere surface. The resonance energies were also dependent on the geometrical parameters (Ag size, contact angles, ..) but stay in the above mentioned range. Such interface plasmon resonance between a plasmonic metallic particle and an oxide substrate with a high refractive index were reported in the case of silver [49] or gold [32] particles on titania. Both works indicated that the hot spot at the interface region can be strongly red shifted with respect to the metal resonance. The size-dependence on the metal particle of the light intensity enhancement was also theoretically reported by Wei et al.[32] A similar interfacial effect is then expected for silver particles on ceria (refractive index n: 2.2–2.8) and explain the strong resonance at the corner.

Accordingly, the promising SERS effect can be explained by two mechanisms. The first mechanism is the plasmonic features of the composites. The EELS analysis demonstrates that small Ag NPs can have a hot-spot with proper inter-particle spacing for good SERS activity. It also shows that large silver particles can have an interfacial plasmon mode with the ceria whose resonance energy (2.1 - 2.5eV) is in the excitation laser energy range (2.33 eV) and in the absorption energy ranges of the rhodamine (ca. 2.3 eV). Those two combined plasmonic effects result in an immense enhancement in the Raman scattering signals. In sample IV, the Ag particle coverage seems optimum to obtain the benefit of the two plasmonic effects.

The other mechanism is the composites morphology made of a supporting hollow ceria sphere. Such a hollow structure provides buoyant ability and the wide size distribution improves dispersion in solution, both results in contact probability enhancement with the molecule. This concept, called

Published on 07 January 2019. Downloaded on 1/21/2019 12:35:13 AM.

Nanoscale Accepted Manuscript

View Article Online
DOI: 10.1039/C8NR09636H

lab-on-a-bubble (LoB), was already reported in order to overcome the poor reproducibility of mobile NPs, which is due to the Brownian motion of nanoparticles in solution.[33, 44] It was based on low-density microspheres that utilize buoyant force to drive assay separation. Carron et al. showed a promising SERS effect in hollow buoyant $SiO_2$ microspheres.[33] In this study, a different type of buoyant substrate was demonstrated.

## Conclusion

This study demonstrated a new composite with RTFM and distinguished SERS effect. Hollow $CeO_2$-Ag core-shell structure composite, H-$CeO_2$@Ag, was synthesized successfully using a two-step process. The hollow $CeO_2$ sphere diameter ranges from 100 nm to 2 μm, while the shell thickness is about 30 nm. Ag NPs with sizes varying from 5 to 50 nm were deposited homogeneously onto the surface of $CeO_2$ spheres. The Ag deposition process results in $Ce^{3+}$ aggregation that lead to FM enhancement.

The micro-feature of Ag NPs on $CeO_2$ spheres satisfies the criteria of silver based NPs hot-spots and also induces a new plasmon mode at the interface, showing that all H-$CeO_2$@Ag samples provided enhanced SERS effect. With optimum size and inter-particle spacing of Ag NPs, the detection limit was found to be as high as $1\times10^{-14}$ M with the EF was $4.8\times10^{11}$. The multifunctionality of these composites provides applications in biosensors, electric devices, photocatalytic cells and photo detectors.

## Acknowledgement

This research is supported by the Ministry of Science and Technology of Taiwan, Republic of China, under Contract No. MOST 104-2112-M-011 -001 -MY3. We would also like to give special thanks to Dr. Mathieu Kociak in the discussion of plasmon analysis.

## References

1. Yang, Z.; Woo, T. K.; Baudin, M.; Hermansson, K. *The Journal of Chemical Physics* **2004,** 120, (16), 7741-7749.
2. Chen, S.-Y.; Lu, Y.-H.; Huang, T.-W.; Yan, D.-C.; Dong, C.-L. *The Journal of Physical Chemistry C* **2010,** 114, (46), 19576-19581.
3. Carrettin, S.; Concepción, P.; Corma, A.; López Nieto José, M.; Puntes Victor, F. *Angewandte Chemie International Edition* **2004,** 43, (19), 2538-2540.
4. Steele, B. C. H.; Heinzel, A. *Nature* **2001,** 414, 345.
5. Fu, Q.; Saltsburg, H.; Flytzani-Stephanopoulos, M. *Science* **2003,** 301, (5635), 935.
6. Bera, P.; Patil, K. C.; Hegde, M. S. *Physical Chemistry Chemical Physics* **2000,** 2, (16), 3715-3719.

Published on 07 January 2019. Downloaded on 1/21/2019 12:35:13 AM.

Nanoscale Accepted Manuscript

View Article Online
DOI: 10.1039/C8NR09636H

7. Machida, M.; Murata, Y.; Kishikawa, K.; Zhang, D.; Ikeue, K. *Chemistry of Materials* **2008,** 20, (13), 4489-4494.

8. Heo, I.; Schmieg, S. J.; Oh, S. H.; Li, W.; Peden, C. H. F.; Kim, C. H.; Szanyi, J. *Catalysis Science & Technology* **2018,** 8, (5), 1383-1394.

9. Vayssilov, G. N.; Lykhach, Y.; Migani, A.; Staudt, T.; Petrova, G. P.; Tsud, N.; Skála, T.; Bruix, A.; Illas, F.; Prince, K. C.; Matolı´n, V. r.; Neyman, K. M.; Libuda, J. *Nature Materials* **2011,** 10, 310.

10. Wang, Y.-G.; Mei, D.; Glezakou, V.-A.; Li, J.; Rousseau, R. *Nature Communications* **2015,** 6, 6511.

11. Kim, H. Y.; Lee, H. M.; Henkelman, G. *Journal of the American Chemical Society* **2012,** 134, (3), 1560-1570.

12. Outka, D. A.; Stöhr, J.; Jark, W.; Stevens, P.; Solomon, J.; Madix, R. J. *Physical Review B* **1987,** 35, (8), 4119-4122.

13. Gravil, P. A.; Bird, D. M.; White, J. A. *Physical Review Letters* **1996,** 77, (18), 3933-3936.

14. Chen, S.-Y.; Tseng, E.; Lai, Y.-T.; Lee, W.; Gloter, A. *Nanoscale* **2017,** 9, (30), 10764-10772.

15. Chang, S.; Ruan, S.; Wu, E.; Huang, W. *The Journal of Physical Chemistry C* **2014,** 118, (33), 19238-19245.

16. Chen, S.-Y.; Tsai, C.-H.; Huang, M.-Z.; Yan, D.-C.; Huang, T.-W.; Gloter, A.; Chen, C.-L.; Lin, H.-J.; Chen, C.-T.; Dong, C.-L. *The Journal of Physical Chemistry C* **2012,** 116, (15), 8707-8713.

17. Lee, W.; Chen, S.-Y.; Chen, Y.-S.; Dong, C.-L.; Lin, H.-J.; Chen, C.-T.; Gloter, A. *The Journal of Physical Chemistry C* **2014,** 118, (45), 26359-26367.

18. Lv, J.; Fang, M.; Liu, Y. *Journal of Alloys and Compounds* **2017,** 721, 633-637.

19. Chen, S.-Y.; Fong, K.-W.; Peng, T.-T.; Dong, C.-L.; Gloter, A.; Yan, D.-C.; Chen, C.-L.; Lin, H.-J.; Chen, C.-T. *The Journal of Physical Chemistry C* **2012,** 116, (50), 26570-26576.

20. Lee, W.; Chen, S.-Y.; Tseng, E.; Gloter, A.; Chen, C.-L. *The Journal of Physical Chemistry C* **2016,** 120, (27), 14874-14882.

21. Coey, J. M. D.; Venkatesan, M.; Fitzgerald, C. B. *Nature Materials* **2005,** 4, 173.

22. Coey, J. M. D.; Stamenov, P.; Gunning, R. D.; Venkatesan, M.; Paul, K. *New Journal of Physics* **2010,** 12, (5), 053025.

23. Coey, M.; Ackland, K.; Venkatesan, M.; Sen, S. *Nature Physics* **2016,** 12, 694.

24. Deng, S.; Loh, K. P.; Yi, J. B.; Ding, J.; Tan, H. R.; Lin, M.; Foo, Y. L.; Zheng, M.; Sow, C. H. *Applied Physics Letters* **2008,** 93, (19), 193111.

25. Jiang, Z.; Chen, S.; Zhang, D. *The Journal of Physical Chemistry C* **2014,** 118, (7), 3789-3794.

26. Esch, F.; Fabris, S.; Zhou, L.; Montini, T.; Africh, C.; Fornasiero, P.; Comelli, G.; Rosei, R. *Science* **2005,** 309, (5735), 752.

27. Škoda, M.; Cabala, M.; Matolínová, I.; Prince, K. C.; Skála, T.; Šutara, F.; Veltruská, K.; Matolín, V. *The Journal of Chemical Physics* **2009,** 130, (3), 034703.

28. Ou, D. R.; Mori, T.; Togasaki, H.; Takahashi, M.; Ye, F.; Drennan, J. *Langmuir* **2011,** 27, (7), 3859-3866.

Published on 07 January 2019. Downloaded on 1/21/2019 12:35:13 AM.

Nanoscale Accepted Manuscript

View Article Online
DOI: 10.1039/C8NR09636H

29. Chen, L.; Sun, H.; Zhao, Y.; Zhang, Y.; Wang, Y.; Liu, Y.; Zhang, X.; Jiang, Y.; Hua, Z.; Yang, J. *RSC Advances* **2017,** 7, (27), 16553-16560.

30. Gao, N.; Chen, Y.; Jiang, J. *ACS Applied Materials & Interfaces* **2013,** 5, (21), 11307-11314.

31. Liu, H.; Yang, W.; Wang, M.; Xiao, L.; Liu, S. *Sensors and Actuators B: Chemical* **2016,** 236, 490-498.

32. Wei, Z.; Rosa, L.; Wang, K.; Endo, M.; Juodkazis, S.; Ohtani, B.; Kowalska, E. *Applied Catalysis B: Environmental* **2017,** 206, 393-405.

33. Schmit, V. L.; Martoglio, R.; Scott, B.; Strickland, A. D.; Carron, K. T. *Journal of the American Chemical Society* **2012,** 134, (1), 59-62.

34. A. Nakajima, A. Yoshihara, and M. Ishigame, "Defect-induced Raman spectra in doped $CeO_2$," *Physical Review B,* vol. 50, pp. 13297-13307, 1994.

35. Maitra, U.; Das, B.; Kumar, N.; Sundaresan, A.; Rao, C. N. R. *ChemPhysChem* **2011,** 12, (12), 2322-2327.

36. Tahir, N.; Karim, A.; Persson, K. A.; Hussain, S. T.; Cruz, A. G.; Usman, M.; Naeem, M.; Qiao, R.; Yang, W.; Chuang, Y.-D.; Hussain, Z. *The Journal of Physical Chemistry C* **2013,** 117, (17), 8968-8973.

37. Marenco, A. J.; Pedersen, D. B.; Trudel, S. *Journal of Materials Chemistry C* **2017,** 5, (20), 4899-4908.

38. Li, M.; Ge, S.; Qiao, W.; Zhang, L.; Zuo, Y.; Yan, S. *Applied Physics Letters* **2009,** 94, (15), 152511.

39. Rodríguez-Lorenzo, L.; Álvarez-Puebla, R. A.; Pastoriza-Santos, I.; Mazzucco, S.; Stéphan, O.; Kociak, M.; Liz-Marzán, L. M.; García de Abajo, F. J. *Journal of the American Chemical Society* **2009,** 131, (13), 4616-4618.

40. Israelsen, N. D.; Hanson, C.; Vargis, E. *The Scientific World Journal* **2015,** 2015, 12.

41. Tian, F.; Bonnier, F.; Casey, A.; Shanahan, A. E.; Byrne, H. J. *Analytical Methods* **2014,** 6, (22), 9116-9123.

42. Hildebrandt, P.; Stockburger, M. *The Journal of Physical Chemistry* **1984,** 88, (24), 5935-5944.

43. Kim, K.; Han, H. S.; Choi, I.; Lee, C.; Hong, S.; Suh, S.-H.; Lee, L. P.; Kang, T. *Nature Communications* **2013,** 4, 2182.

44. Jiang, J.; Ou-Yang, L.; Zhu, L.; Zou, J.; Tang, H. *Scientific Reports* **2014,** 4, 3942.

45. Monreal, R. C.; Tomasz, J. A.; Apell, S. P. *New Journal of Physics* **2013,** 15, (8), 083044.

46. Lee, H.-B.-R.; J. Maeng, W.; Kim, M. K.; Gatineau, J.; Kim, H. K., *Electronic Structure of Cerium Oxide Gate Dielectric Grown by Plasma-Enhanced Atomic Layer Deposition*. 2011; Vol. 158, p G217.

47. Chu, M.-W.; Myroshnychenko, V.; Chen, C. H.; Deng, J.-P.; Mou, C.-Y.; García de Abajo, F. J. *Nano Letters* **2009,** 9, (1), 399-404.

48. Koh, A. L.; Bao, K.; Khan, I.; Smith, W. E.; Kothleitner, G.; Nordlander, P.; Maier, S. A.; McComb, D. W. *ACS Nano* **2009,** 3, (10), 3015-3022.

49. Tanabe, I.; Tatsuma, T. *Nano Letters* **2012,** 12, (10), 5418-5421.

Published on 07 January 2019. Downloaded on 1/21/2019 12:35:13 AM.

Nanoscale Accepted Manuscript

View Article Online
DOI: 10.1039/C8NR09636H

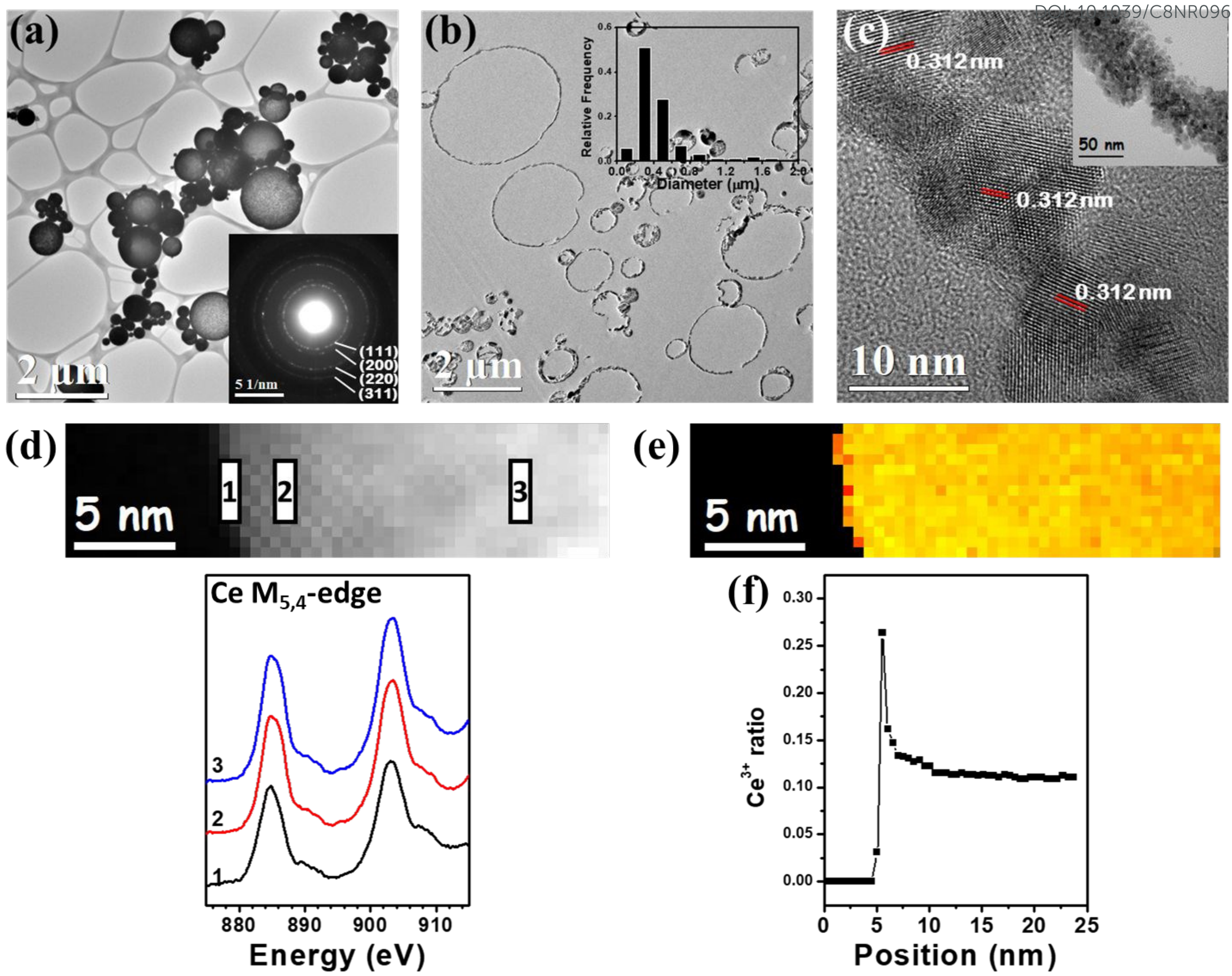

Figure 1. (a) TEM image of $CeO_2$ sphere and its diffraction pattern (inset). (b) TEM image of cross section and size distribution of $CeO_2$ sphere (inset). (c) High-resolution TEM image of $CeO_2$ NPs and the cross-sectional image of $CeO_2$ shell (inset). (d) STEM/HAADF (upper) and EELS mapping of $Ce^{3+}$ of H-$CeO_2$ (lower), the spectra of position 1, 2 and 3 are plotted in (e). The intensity profile of $Ce^{3+}$ is shown in (f).

Published on 07 January 2019. Downloaded on 1/21/2019 12:35:13 AM.

Nanoscale Accepted Manuscript

View Article Online
DOI: 10.1039/C8NR09636H

Published on 07 January 2019. Downloaded on 1/21/2019 12:35:13 AM.

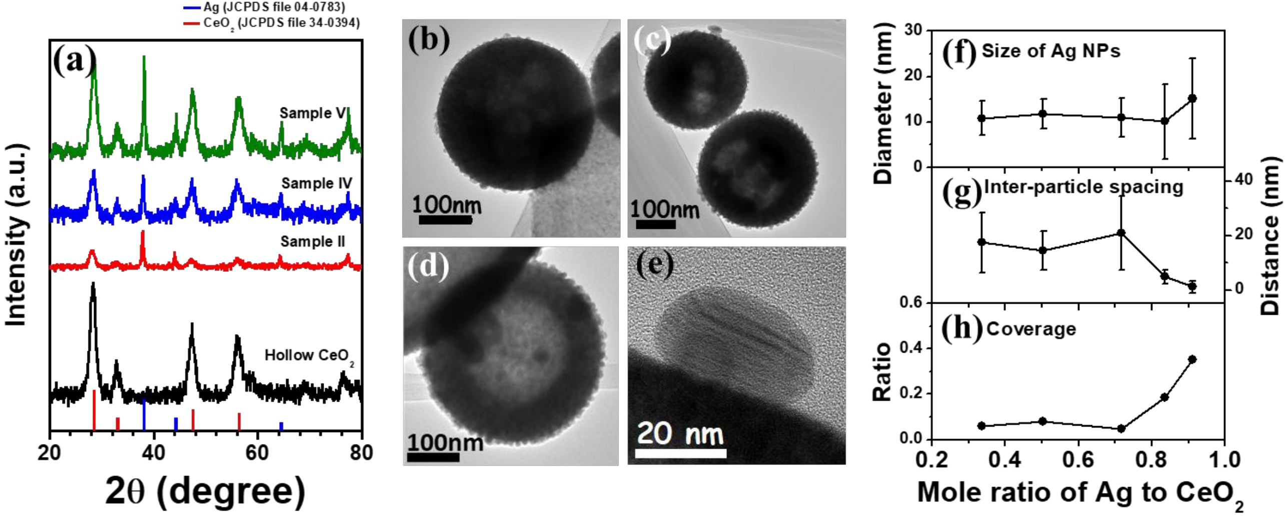

Figure 2 (a) XRD spectra of H-$CeO_2$@Ag sphere with different Ag/Ce ratio. TEM images of sample II (b), IV (c) and V (d) demonstrate that the amount and distribution of Ag on $CeO_2$ varies with concentration. (e) HR-TEM image shows clear interface between Ag and $CeO_2$ sphere. The average size and inter-particle spacing of Ag NPs is shown in (f) and (g). The calculated coverage ratio of Ag on $CeO_2$ sphere is plotted in (h).

Nanoscale Accepted Manuscript

View Article Online
DOI: 10.1039/C8NR09636H

Published on 07 January 2019. Downloaded on 1/21/2019 12:35:13 AM.

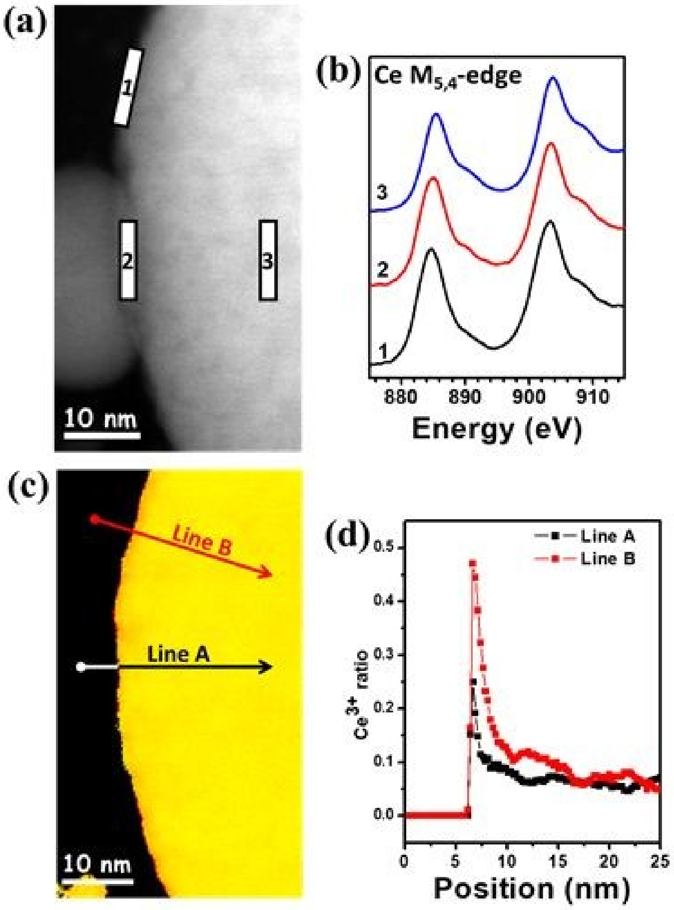

Figure 3. (a) STEM/HAADF of H-CeO$_2$ @Ag, (b) Ce M –edge EELS spectra acquired from position 1 to 3 as indicated in (a). (c) EELS mapping of Ce$^{3+}$ of figure (a), the intensity profile of Ce$^{3+}$ of line A and B are plotted in (d).

Nanoscale Accepted Manuscript

View Article Online
DOI: 10.1039/C8NR09636H

Published on 07 January 2019. Downloaded on 1/21/2019 12:35:13 AM.

Nanoscale Accepted Manuscript

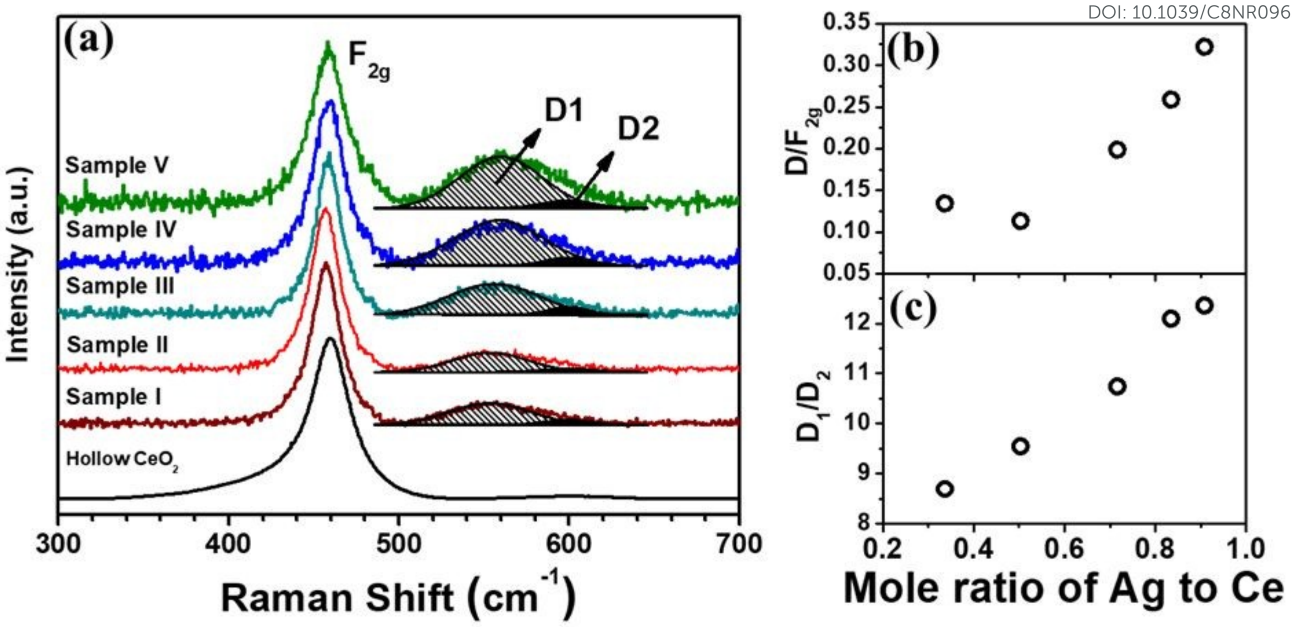

Figure 4 (a) Raman measurement of Ag deposited $CeO_2$ hollow spheres with different Ag/Ce mole ratio. The fitting value on $D/F_{2g}$ and $I_{D1}/I_{D2}$ are plotted in (b) and (c).

View Article Online
DOI: 10.1039/C8NR09636H

Published on 07 January 2019. Downloaded on 1/21/2019 12:35:13 AM.

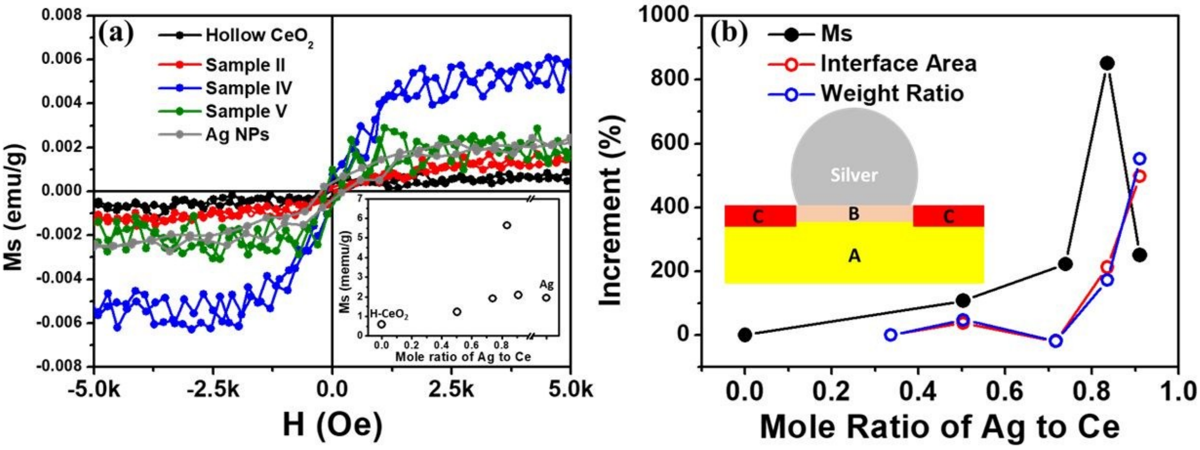

Figure 5. (a) M-H curve of samples I, III, IV, V, and bare Ag. (b) Comparison of the increment of $M_s$, interface area between Ag and H-$CeO_2$@Ag, and weight ratio of Ag/H-$CeO_2$@Ag with changing the Ag/Ce mole ratio.

Nanoscale Accepted Manuscript

View Article Online
DOI: 10.1039/C8NR09636H

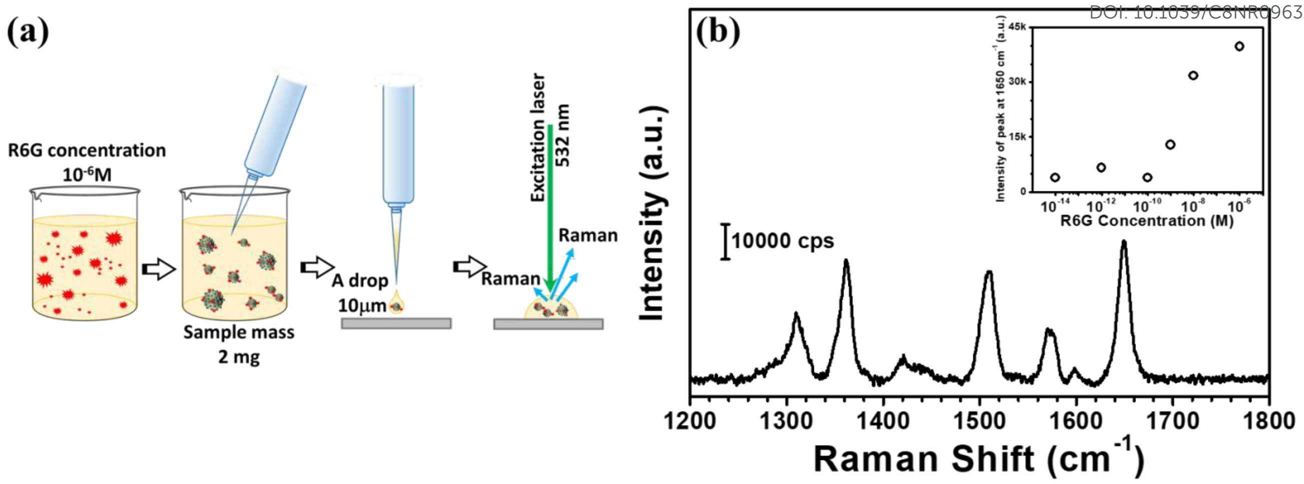

Figure 6. (a) Illustration of measure process of H-$CeO_2$@Ag composites. (b) SERS spectra of $10^{-6}$ M R6G on the sample IV and a logarithmic plot of R6G concentration vs. signal intensity for the band at 1663 $cm^{-1}$ (inset).

Published on 07 January 2019. Downloaded on 1/21/2019 12:35:13 AM.

Nanoscale Accepted Manuscript

View Article Online
DOI: 10.1039/C8NR09636H

Published on 07 January 2019. Downloaded on 1/21/2019 12:35:13 AM.

Nanoscale Accepted Manuscript

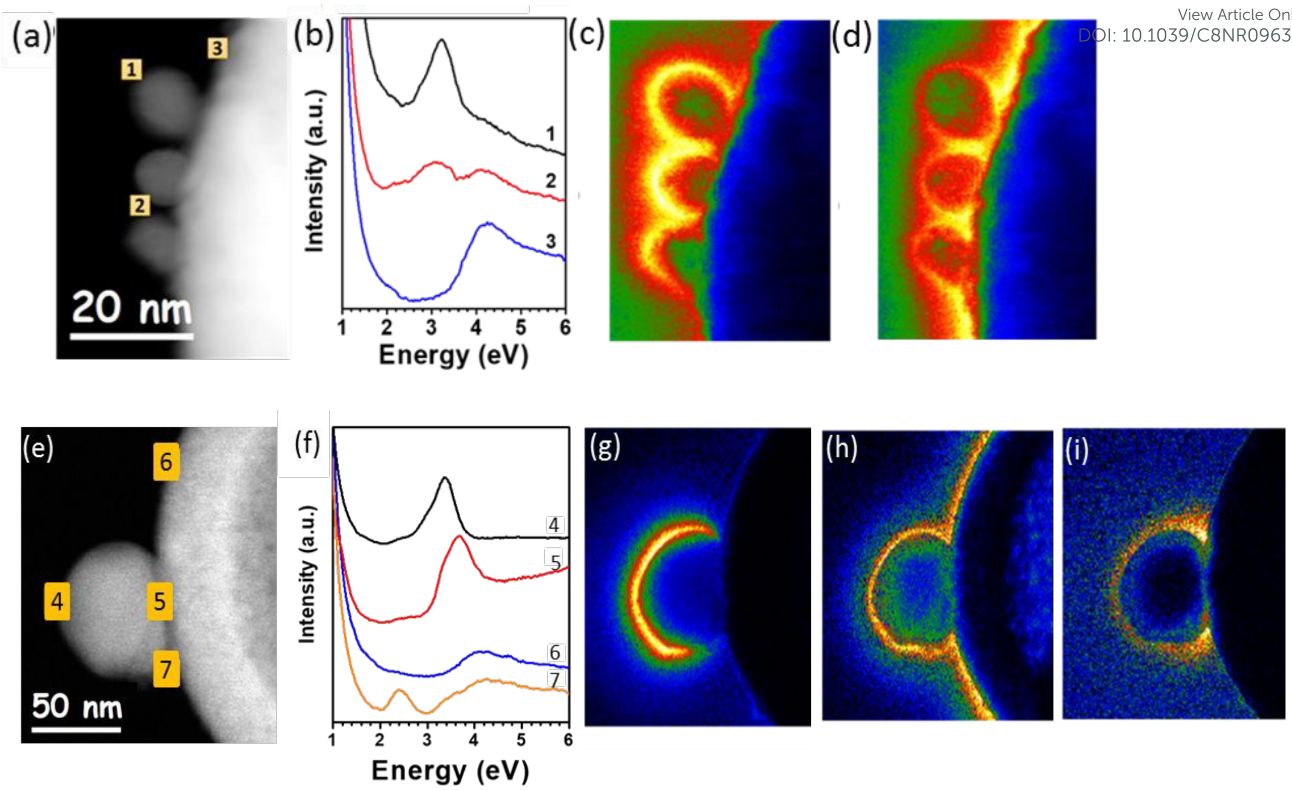

Figure 7. (a) STEM/HAADF image of H-CeO$_2$@Ag composites with small Ag particles on its surface. (b) EELS spectra of different position as indicated in (a). . The EELS intensity spatial distribution for two energy windows: (c) is obtained from 3 to 3.3 eV and (d) is obtained from 4 to 4.3 eV. (e) STEM/HAADF image of H-CeO$_2$@Ag composites with large Ag particles on its surface. (f) EELS spectra of different position as indicated in (e).The EELS intensity spatial distribution for different energy windows. (g) is obtained from 3 to 3.3 eV, (h) is obtained from 4 to 4.3 eV, and (i) is obtained from 2.1 to 2.4 eV.